# Robust Multi-Halide Methylammonium-Free Perovskite Solar Cells on an Inverted Architecture

*Jose J. Jeronimo-Rendon, Silver-Hamill Turren-Cruz,\* Jorge Pascual, Diego Di Girolamo, Marion A. Flatken, Hans Köbler, Wolfram Hempel, Meng Li, Aldo Di Carlo, Pablo P. Boix, Iván Mora-Seró, Antonio Abate, and Michael Saliba\**

Developing efficient wide-bandgap perovskites is critical to exploit the benefits of a multi-absorber solar cell and engineering commercially attractive tandem solar cells. Here, a robust, additive-free, methylammonium-free triple halide composition for the fabrication of close-to-ideal wide-bandgap perovskites (1.64 eV) is reported. The introduction of low percentages of chloride into the perovskite layer avoided photoinduced halide segregation and lead to an evident improvement in the crystallization process, reaching enhanced open-circuit voltages as high as 1.23 V. A perovskite of these characteristics is introduced for the first time in a p-i-n single-junction configuration using a self-assembled monolayer, with devices achieving photoconversion efficiencies of up to 22.6% with ultra-high stability, retaining ≈80% of their initial efficiency after >1000 h of continuous operation unencapsulated in a nitrogen atmosphere at 85 °C. This result paves the way toward highly efficient multi-junction tandem solar cells, bringing perovskite technology closer to commercialization.

## 1. Introduction

Silicon-perovskite tandem solar cells aim to overcome the performance of single junction devices by combining the silicon subcell with a wide-bandgap (WBG) perovskite of around 1.7 eV.

The bandgap of perovskite materials, $ABX_3$, can be easily tuned through the adjustment of the X-site halide content, combining different anions.[1] However, the mixing of halides into the perovskite lattice can lead to photoinduced phase segregation, and non-radiative recombination, thus directly affecting the long-term robustness of the material.[2–4] In addition, most of these perovskites contain methylammonium (MA) in the A-site position, which undergoes widely reported thermally induced degradation mechanisms undermining long-term stability.[5,6] Thus, formamidinium (FA) is usually selected, often in combination with alkali cations like $Cs^+$ or $Rb^+$.[7–9] The main obstacle to the fabrication of high-quality MA-free perovskite thin films is the instability of the $\alpha$-phase in pure FA perovskites and the faster crystallization dynamics in Cs-containing ones.

Therefore, MA-free WBG perovskites simultaneously face two main challenges toward their long-term stability: the phase segregation due to the I–Br content, and the less controlled thin film growth for MA-free compositions. To suppress halide mobility and its consequent segregation, several reports have

J. J. Jeronimo-Rendon, M. Saliba
Institute for Photovoltaics
University of Stuttgart
Pfaffenwaldring 47, 70569 Stuttgart, Germany
E-mail: michael.saliba@ipv.uni-stuttgart.de

J. J. Jeronimo-Rendon, J. Pascual, M. A. Flatken, H. Köbler, M. Li, A. Abate
Department of Novel Materials and Interfaces for Photovoltaic Solar Cells
Helmholtz-Zentrum Berlin für Materialien und Energie
Hahn-Meitner-Platz 1, 14109 Berlin, Germany

S.-H. Turren-Cruz, P. P. Boix
Instituto de Ciencia de los Materiales (ICMUV)
Universitat de Valencia
Paterna 46980, Spain
E-mail: silver.turren@uv.es

The ORCID identification number(s) for the author(s) of this article can be found under https://doi.org/10.1002/adfm.202313928

S.-H. Turren-Cruz
Department of Physical Chemistry
Polish Academy of Sciences
Warsaw 01-224, Poland

J. Pascual
Polymat
University of the Basque Country UPV/EHU
Donostia-San Sebastian 20018, Spain

D. D. Girolamo, A. D. Carlo
Centre for Hybrid and Organic Solar Energy (CHOSE)
Department of Electronic Engineering
University of Rome "Tor Vergata"
Via del Politecnico 1, Roma 00133, Italy

W. Hempel
Zentrum für Sonnenenergie-und Wasserstoff-Forschung
Baden-Württemberg (ZSW)
70563 Stuttgart, Germany

**ADVANCED
SCIENCE NEWS**

www.advancedsciencenews.com

**ADVANCED
FUNCTIONAL
MATERIALS**

www.afm-journal.de

shown the effectiveness of chloride introduction.[10–12] Further benefits include defect passivation[13,14] and the manipulation of the crystallization process of the perovskite thin film.[15–17] For instance, the use of alkylammonium chloride species allowed controlling the growth of $FAPbI_3$ perovskite to obtain photoconversion efficiencies (PCEs) over 26%.[18] Current studies of WBG materials in perovskite-silicon tandem solar cells have achieved high in tandem devices of PCE over 33%, particularly through interfacial modification.[19–21] The next necessary step for the advancement of perovskite tandem technology is thus to provide highly stable WBG MA-free perovskite solar cells. Previous results suggest that compositional engineering could successfully avoid halide segregation in multi-halide WBG perovskites, and simultaneously allow thermally stable MA-free compositions in high quality through the regulation of the thin film crystallization.

In this work, we present a triple halide MA-free composition for fabricating highly stable perovskites with a close-to-ideal bandgap of 1.64 eV. We take advantage of the versatile abilities of chloride ions to simultaneously suppress phase segregation and control crystal growth. The best single junction devices show PCEs of up to 22.6%, and high stability, retaining 89% of its initial value after 1000 h at 25 °C and 80% after 650 h at high temperatures up to 85 °C. These results outperform all previous reports on WBG (in the context of this work, 1.6–1.8 eV), with almost one point PCE improvement (**Figure 1**a) and longest stability at maximum power point tracking (MPPT) at both low and high temperatures (Figure 1b) using ISOS-protocol (International Summit on Organic Photovoltaic Stability). All data is listed in Tables S1 and S2 (Supporting Information). Overall, we present a robust method for the fabrication of efficient WBG MA-free perovskite solar cells with very high stability at high temperatures, providing the tools for the development of efficient and long-term stable tandem devices.



**Figure 1.** Device results of this work as red stars in the context of literature. a) PCEs over 20% of PSCs with an absorber bandgap of 1.6–1.8 eV. b) $T_{80}$ of PSCs with an absorber bandgap of 1.6–1.8 eV during MPPT using ISOS protocol. Unless specified, the measurements were carried out at 20–25 °C.

M. Li
Key Lab for Special Functional Materials
Ministry of Education
National & Local Joint Engineering Research Center for High-efficiency Display and Lighting Technology
School of Materials Science and Engineering
and Collaborative Innovation Center of Nano Functional Materials and Applications
Henan University
Kaifeng 475004, China

I. Mora-Seró
Institute of Advanced Materials (INAM)
University Jaume I
Av. Vicent Sos Baynat, s/n, Castellón de la Plana 12071, Spain

A. Abate
Department of Chemical
Materials and Production Engineering
University of Naples Federico II
Naples
pzz.le Vincenzo Tecchio 80, Naples 80125, Italy

M. Saliba
Helmholtz Young Investigator Group FRONTRUNNER
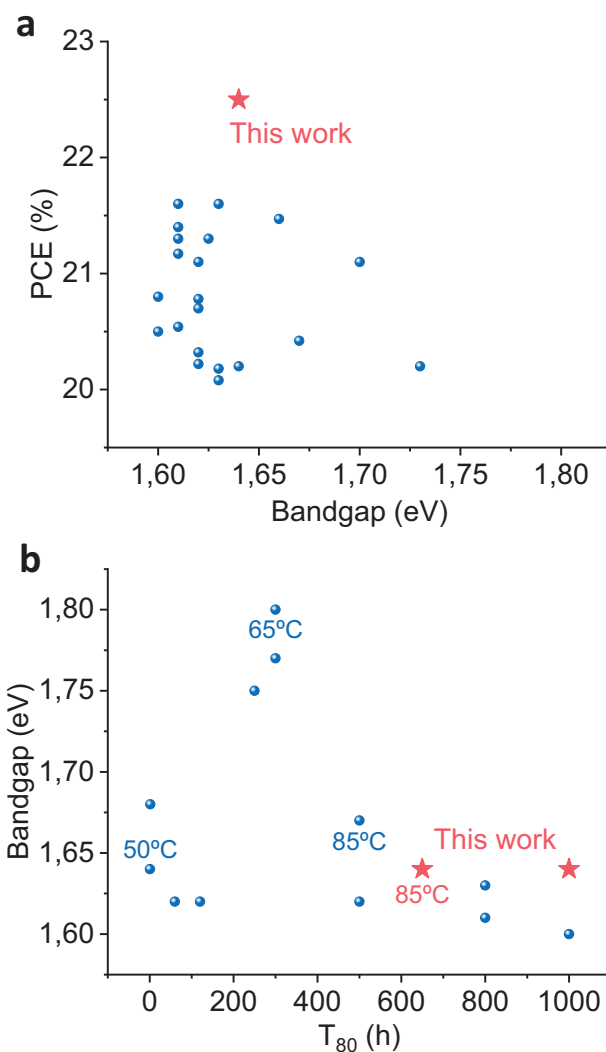IEK5-Photovltaics Forschungszentrum Jülich
52425 Jülich, Germany

## 2. Results and Discussion

We prepared, through a solution-based process, see Supporting Information (SI) for further details, three different perovskite compositions varying their halide content: $Cs_{0.1}FA_{0.9}PbI_3$ as single halide, $Cs_{0.2}FA_{0.8}Pb(I_{0.82}Br_{0.18})_3$ as double halide, and $Cs_{0.2}FA_{0.8}Pb((I_{0.82}Br_{0.18})_{0.97}Cl_{0.03})_3$ as triple halide, respectively, abbreviated for convenience as CsFA-I, CsFA-IBr, and CsFA-IBrCl. The reason to use different Cs contents for single and multiple halide perovskites originates from reported studies but also from previous experience,[22,23] where 10% Cs as the A-site cation is sufficient to allow the right phase formation for $FAPbI_3$-based perovskite. Increasing the amount of Cs is of interest as it can increase the intrinsic stability of the material. However, too high Cs content leads to its agglomeration, causing lower reproducibility, morphology, and crystallinity for $FAPbI_3$-based

**ADVANCED
SCIENCE NEWS**

www.advancedsciencenews.com

**ADVANCED
FUNCTIONAL
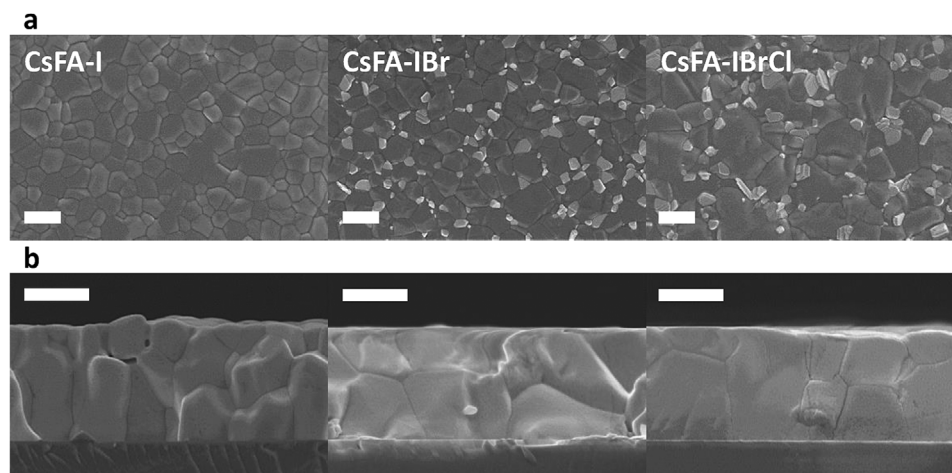MATERIALS**

www.afm-journal.de

**Figure 2.** a) Top and b) cross-section SEM images of perovskite films with the different halide compositions. The scale bars represent 500 nm.

perovskites, negative effects that are avoided for Br-containing (FAPb(IBr)$_3$) materials. Cs tends to distort the perovskite structure at high ratios when only iodide present, but bromide favors thermodynamically the right phases in these situations.[22] Then, we initially set the bromide content at 18% as it provides a close-to-ideal bandgap, though further optimization of the halide ratios will be carried out ahead. Finally, we selected the chloride content of 3% after we obtained the largest grains with it by scanning electron microscopy (SEM), in contrast with higher amounts like 5 or 10%, see Figure S1 (Supporting Information).

To investigate the influence of the halide content in the crystallization of the material, we first fabricated thin films of these compositions on glass/ITO/2PACz (where ITO is indium tin oxide, and 2PACz is [2-(9H-carbazol-9-yl)ethyl]phosphonic acid as a self-assembled monolayer on the contact surface). We analyzed these thin films by SEM, finding compact surfaces with no pinholes for the top view measurements, see **Figure 2a**. There was however a significant increase in the grain size from CsFA-I to CsFA-IBr and CsFA-IBrCl, particularly for the latter. We calculated the grain size distribution from the images, Figure S2 (Supporting Information), and estimated an increase in the average value from 250 and 340 nm for the single and double halide perovskites, respectively, to 710 nm for triple halide perovskite. This also led to a wider distribution range for the grain sizes for multiple halide perovskites, being most of the grains 200–400 nm for single halide, 200–500 nm for double halide, and 400–1000 nm for triple halide. The top images also showed the presence of bright particles of ≈100 nm on the surface of the double and triple halide perovskite films. A potential origin of these formations is the accumulation of PbI$_2$ in this region of the film, which we will be able to further analyze by studying their crystalline properties, see below. Meanwhile, the cross-section SEM images showed a comparable thickness of ≈900 nm for all the films, see Figure 2b. We observed, however, a main difference in the vertical distribution of the grains. Single and double halide perovskites presented grains located on top of each other, implying that photogenerated charges may encounter grain boundaries on their way to the extraction interfaces, reducing the effectiveness of charge collection. In this regard, triple halide composition led to monolithically thin films, with grains stretching from the buried interface

to the top surface. This has positive implications on the thin film quality, suggesting a more efficient transport of the charges in the triple halide material. Overall, the SEM results clearly point out the positive influence of chloride insertion in the perovskite thin film formation, leading to a vast increase in the grain size, as well as in the formation of monolithic and compact grains for thicknesses approaching 1 μm.

To analyze the crystalline properties of the films, we measured them by X-ray diffraction (XRD). As we show in **Figure 3a**, all the films have very similar XRD patterns and present the same peaks. Figure S3 (Supporting Information) shows the assignment of the corresponding reflections for each peak, being the most intense one associated with the 100 reflection at ≈14°. The main perovskite diffraction peaks shift to larger angles when introducing further halides, attributed to the expansion of the lattice, see Figures S3, S4, and Table S3 (Supporting Information). There is a shift of 0.2–0.4° after inserting bromide in the lattice. Interestingly, the addition of chloride also leads to a small shift compared to the double halide perovskite, suggesting also the inclusion of this halide into the crystal. The full width at half maximum (FWHM) values of the peaks slightly increased after the addition of more than one halide, see Table S3 (Supporting Information). The addition of chlorine ions to the perovskite solution has a clear effect on enlarging the grain size, which reduces the density of grain boundaries and facilitates charge transport throughout the absorber. However, XRD analysis reveals an increase in the unreacted PbI$_2$ peak intensity when adding Cl ions to form CsFA-IBrCl perovskite, as compared to CsFA-I and CsFA-IBr results. This phenomenon can be attributed to an excess of dimethyl sulfoxide (DMSO) in the perovskite solution by the addition of PbCl$_2$ as a precursor solution (see Experimental Section). The increased of DMSO content as a solvent leads to the formation of intermediate phases with PbI$_2$. Nevertheless, a higher DMSO content can also result in more PbX$_2$-DMSO intermediates, which can stretch the PbI$_2$ lattice larger, ultimately leading to a more thorough formation of the perovskite.[24] The bright crystals are identified on the perovskite surface by SEM indicating areas of higher electron density, where charges accumulate during measurement. The bright crystals are mainly composed of a mixture of lead iodide and bromide (PbX$_2$, where X is a combination of

**ADVANCED
SCIENCE NEWS**
www.advancedsciencenews.com
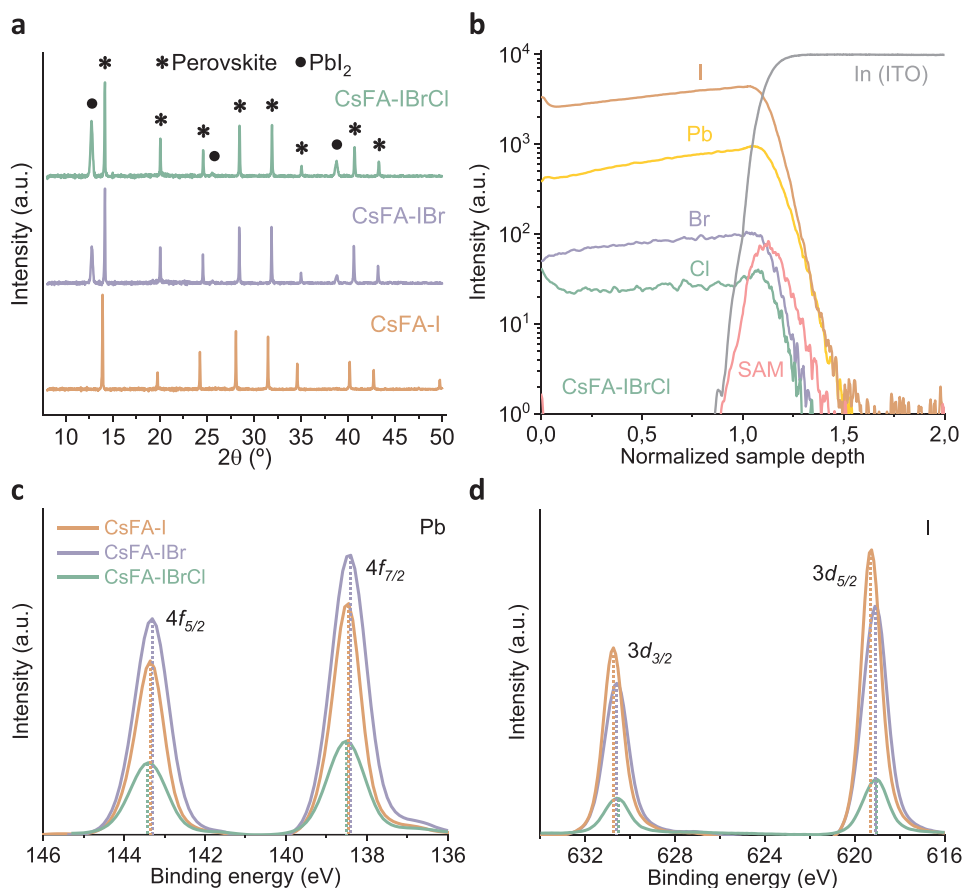
**ADVANCED
FUNCTIONAL
MATERIALS**
www.afm-journal.de

**Figure 3.** a) XRD results of perovskite thin films with different compositions. b) ToF-SIMS results of depth-dependent material content for CsFA-IBrCl triple halide perovskite. The Cs trace is absent due to the utilization of a Cs ion beam during sputtering, which boosted signal intensities. c) XPS spectra of perovskite thin films with different compositions for the ranges of Pb 4f and d) I 3d signals.

halides).[25] It is widely recognized that lead halides are characterized by a higher electron density, mainly due to the absence of organic molecules to reduce their electron density. This plays an essential role in determining the performance of the PSCs. In comparison to perovskite with MA, where the phase segregation is most likely related to the fast release of organic material as MA.[26] However, the impact of this $PbI_2$ content on the potential photovoltaic performance of these thin films is unclear. While some reports suggest it can degrade to $Pb^0$ and $I_2$ through photolysis and induce interstitial defects,[27,28] a small excess of $PbI_2$ can also effectively passivate defects and enhance charge extraction and stability.[29,30] These aspects will be discussed in the following sections on photovoltaic devices, see below. Therefore, though triple halide compositions showed a clear improvement in the morphology of the thin films, the insertion of chloride seems to cause no apparent advantage for the crystalline properties.

To study more in-depth the role of chloride in the triple halide composition, we aimed to determine its location in the film and any possible depth dependency. We measured the thin films of the three compositions by time-of-flight secondary ion mass spectrometry (ToF-SIMS), finding a homogeneous distribution throughout the thin film of all perovskite and halide materials. It also indicates a more preferential distribution of $PbI_2$ in both the

bulk and the lower interface in CsFA-IBr and CsFA-IBrCl films, see Figure 3b and Figure S5 (Supporting Information). While the aggregation of this material is only noticeable by SEM on the top surface of perovskite films, these findings suggest that multiple halide perovskite compositions favor the formation of $PbI_2$ at the different film surfaces, i.e., grain boundaries and interfaces. In addition, we identified a slight preference for chloride for the top and bottom interfaces. These results suggest that, apart from assisting in the perovskite crystallization for larger and more compact grain formation, chloride is a potential defect passivator that is preferentially placed at the interfaces (i.e., buried and top surfaces, and grain boundaries). We then analyzed the samples by X-ray photoelectron spectroscopy (XPS), which can offer information on the environment of the different elements present on the thin film surface. First, the Cl 2p signal was found only for the triple halide film, see Figure S6a (Supporting Information), pointing out its presence in the film and on the surface, in agreement with ToF-SIMS results. The Pb 4f and I 3d signals in Figure 3c,d showed a slight shift of ≈0.1 eV for the triple halide thin film with respect to single and double halide samples, suggesting some influence of chloride in the environment of the main perovskite components. This effect is clearer in the C, N, and Cs spectra, see Figure S6b–d (Supporting Information), where the shift goes up to 0.5 eV, but for both double and triple
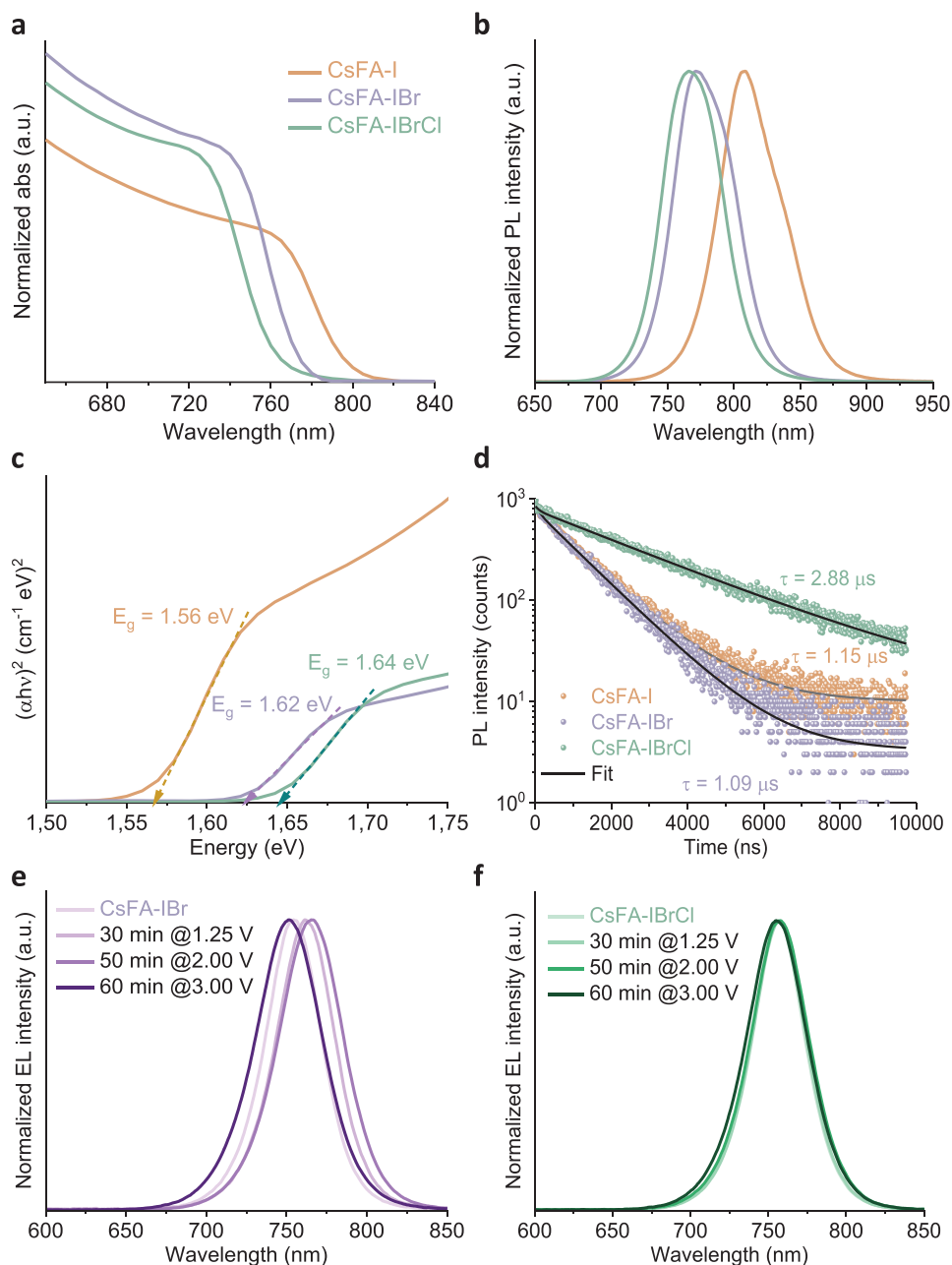
**Figure 4.** a) Absorbance spectra, b) steady-state PL spectra, and c) Tauc plot and bandgap calculation for thin films of the three different compositions. d) TRPL spectra and fit for one, double, and triple halide perovskite thin films. Normalized EL spectra at 1.25, 2, and 3 V for up to 1 h of e) double halide and f) triple halide thin films.

halide samples, thus the bromide and chloride contributions on the A-site cations cannot be differentiated here. According to the results in Pb and I spectra, we anticipate the ability of chloride to passivate undercoordinated centers at the different surfaces.

We then characterized the optoelectronic properties of the fabricated films to investigate the benefits of chloride insertion and its role in defect passivation and stability enhancement. The UV–vis absorption spectra in **Figure 4a** shows single halide perovskite film exhibited the highest absorption among all the films. The absorption band edge shifted to higher wavelengths when bromide

was inserted and, interestingly, chloride further enhanced that shift. These findings are consistent with the steady-state photoluminescence (PL), showing the blue shift of the perovskite PL signal as smaller halides were inserted in the composition, see Figure 4b, from 810 nm for single halide to 770 and 760 nm for double and triple halide, respectively. To obtain an estimation of the bandgap, we calculated the Tauc plot, for a direct semiconductor band gap, presented in Figure 4c. This plot confirms the significant widening of the bandgap from 1.56 eV for single halide perovskite to 1.62 eV for double halide and 1.64 eV

**ADVANCED
SCIENCE NEWS**

www.advancedsciencenews.com

**ADVANCED
FUNCTIONAL
MATERIALS**

www.afm-journal.de

for triple halide. Therefore, just through the incorporation of a small amount of chloride in the perovskite composition, we effectively fabricated a WBG perovskite with a close-to-ideal bandgap for tandem applications. To implement WBG perovskites in solar cells, we investigated any additional benefits of the CsFA-IBrCl composition over the CsFA-IBr one. Fitted time-resolved photoluminescence (TRPL) spectra supported the enhancement of the charge-carrier dynamics associated with the different perovskite film compositions. As expected, the CsFA-IBrCl film exhibited a superior lifetime (2.88 μs) compared to the CsFA-I and CsFA-IBr (1.15 and 1.09 μs), respectively. Therefore, the CsFA-IBrCl perovskite film significantly prolonged the recombination time of the generated carriers, leading to a longer diffusion length of charge carriers. This result suggests the reduction of trap-assisted recombination processes, highlighting the benefits of chloride in decreasing the defects in the perovskite layer, in line with what structural characterization anticipated in Figure 3. Finally, we studied the stability to phase segregation of the WBG perovskites, as candidates for it due to their multiple halide content. To that end, we analyzed the two samples by electroluminescence spectroscopy (EL), applying voltages of up to 3 V for 1 h. For the case of double halide CsFA-IBr perovskite, see Figure 4e, we observed a red-shift in the EL spectra after the application of up to 2 V, an indication of phase segregation being triggered in the perovskite structure. Interestingly, after the application of 3 V for 1 h, the peak position in the EL spectrum blue-shifted back close to its original position. Some reports have introduced the reversible character of halide segregation in metal halide perovskite materials in specific conditions,[31] a scenario reasonably applicable to the present sample. However, this reversibility cannot avoid the eventual generation of defects derived from the phase segregation and the consequent degradation of the material. Meanwhile, the triple halide CsFA-IBrCl sample did not shift went subjected to the same stress, even for prolonged times at 3 V, showing no hint of phase segregation (Figure 4f). From these results, we conclude that chloride insertion in the structure effectively inhibits halide segregation in bromide-containing perovskites, for the bromide content analyzed, opening the door to stable WBG perovskite solar cells. To validate the occurrence of light-induced phase segregation, we conducted PL measurements with a focus on time and intensity dependencies, employing continuous wave laser illumination at 405 nm in an $N_2$ environment. A red shift or the emergence of a lower-energy peak in the PL spectrum signifies the development of light-induced low-bandgap I-rich trap states. During a 20 min exposure to 10-sun–equivalent illumination, CsFA-IBr displayed low-energy PL peaks accompanied by an increase in peak width (Figure S7a, Supporting Information). In contrast, films with triple-halide compositions exhibited no formation of low-energy peaks, maintaining their PL spectral profile and indicating superior photostability (Figure S7b, Supporting Information). At an ultrahigh injection level of 100 suns, CsFA-IBr displayed a more pronounced red shift and broadening of the PL peak (Figure S7c, Supporting Information), albeit much milder than that observed in MA-containing samples, as demonstrated by Xu et al.[32] However, surprisingly, triple-halide films exhibited a PL blue shift, contrary to the expected red shift, attributed to emission growth at the high-energy shoulder of the PL spectrum (Figure S7d, Supporting Information). This uncommon PL blue shift in wide-band gap perovskites at high injection

levels suggests that the incorporation of Cl into the lattice influences the optoelectronic properties and the pathways of halide phase segregation.

To evaluate the photovoltaic performance of these improved perovskite layers, we incorporated them in p-i-n devices in the structure presented in **Figure 5a**: glass/ITO/2PACz/perovskite/$C_{60}$/BCP/Ag (where BCP is bathocuproine and 2PACz is a self-assembled monolayer,[33] and we show the respective energy level diagrams of the fabricated perovskite devices (see Figure S8, Supporting Information). We measured the current density–voltage ($J$–$V$) characteristics to obtain the photovoltaic parameters of the devices. To start, we prepared CsFA-IBrCl-based solar cells with varying chloride concentrations. The results in Figure S9 (Supporting Information) confirm that 3% of chloride leads to the best-performing devices, agreeing with morphological properties in Figure S1 (Supporting Information). Too high chloride content dramatically decreases the short-circuit current density ($J_{SC}$), due to a widening of the bandgap leading to many photons transmitted under AM1.5G. We also optimized the processing conditions and looked for the solution concentration leading to the highest PCE values. The data in Figure S10 (Supporting Information) points to 1.6 м as the optimum condition. Higher concentration conditions performance decreased as they did not lead to homogeneous and compact layers. Interestingly, increasing the solution concentration led to a decrease in open-circuit voltage ($V_{OC}$) and a notable increase in $J_{SC}$ (as seen in Figure S9, Supporting Information). We confirmed the wider absorption range and higher external quantum efficiency (EQE) for the devices at 1.6 м, see Figure S11 (Supporting Information), pointing out the importance of controlling the processing conditions, particularly in the presence of multiple halides, to obtain the desired thin film properties. We also aimed to increase the bromide content in the multiple halide perovskites, to widen the bandgap as much as possible without affecting the PCE. However, for both double and triple halide perovskites, increasing the bromide content from 18% to 20% led to a general decrease in cell performance, see Figures S12 and S13 (Supporting Information). We anticipate other properly adapted types of compositional engineering to efficiently process higher bromide content perovskites. We thus continued using the same $I_{0.82}Br_{0.18}$ ratio.

We then compared the devices based on the single, double, and triple halide perovskite compositions, see Figure S14 (Supporting Information). In line with the optical characterization, the single halide CsFA-I perovskite led to the highest $J_{SC}$ values but underperformed in $V_{OC}$ and fill factor (FF), apart from low reproducibility. The double halide CsFA-IBr perovskite, though with lower $V_{OC}$, presented a much better performance overall. Nevertheless, the addition of chloride to produce triple CsFA-IBrCl perovskite led to a notable enhancement of the $V_{OC}$ and FF. The significant increase in FF may stem from a much more efficient charge transport and extraction, due to the clear improvement in morphological properties for chloride-containing thin films. In fact, the champion device achieved a $V_{OC}$ and FF of 1.23 V and 79.9%, respectively, and a much higher PCE of 22.6% compared to 19.2% and 20.6% for single and double halide perovskite solar cells with stabilized efficiency for each at 180 s, see Figure 5b, Figure S15 (Supporting Information), and **Table 1**. Furthermore, the addition of chloride largely suppresses

**ADVANCED**
**SCIENCE NEWS**
www.advancedsciencenews.com

**ADVANCED**
**FUNCTIONAL**
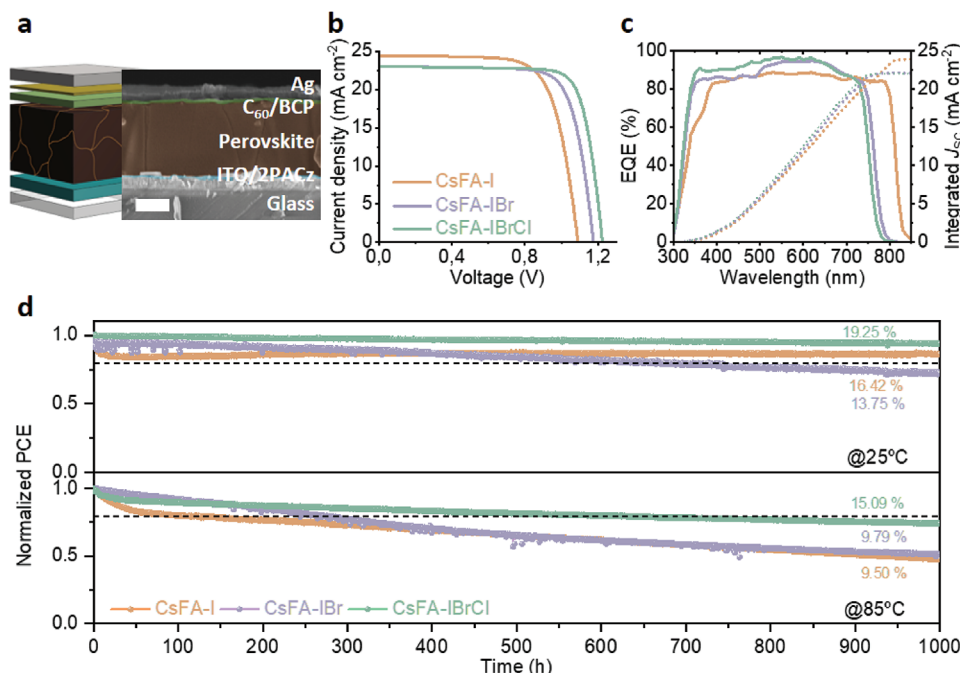**MATERIALS**
www.afm-journal.de

**Figure 5.** a) Full p-i-n device structure and cross-section SEM. b) J–V curves of the champion devices in the reverse scan. c) EQE spectra (left Y axis) and integrated $J_{SC}$ (right Y axis). d) MPPT under 100 mW cm$^{-2}$ light irradiation unencapsulated in N$_2$ atmosphere at 25 and 85 °C. T$_{80}$ is denoted with a dashed line.

the hysteresis present in double and, particularly, single halide devices. The EQE results in Figure 5c agree with the J--V results and both show comparable $J_{SC}$ values within the range. The high crystallinity and good morphology of CsFA-IBrCl perovskite film aided in reducing nonradiative recombination losses of photo-generated carriers by decreasing the presence of grain boundaries and other defects in the lattice. Moreover, there is a possibility that CsFA-I, which has a smaller grain size, may exhibit variances in its electrical properties due to a thinner absorber layer.

Considering the great performance of the triple halide composition in devices, we prepared a large active area device of 1 cm$^2$ see Figure S16 (Supporting Information), one order larger than the 0.18 cm$^2$ ones used above. The champion device achieved a $V_{OC}$ of 1.18 V, a $J_{SC}$ of 21.4 mA cm$^{-2}$, a FF of 71.7%, and a PCE of 18.1%, see Figure S17, Table S4 (Supporting Information). The MPPT showed no losses during the measurement, and in fact increased up to 19% of PCE after 300 s due to the light soaking effect. These results further highlight the potential of the

triple halide strategy as an effective methodology to process high-efficiency WBG perovskites in large-area devices.

Presently, the most formidable endurance test for PSCs is the combined exposure to light and heat stress, known as the International Summit on Organic Photovoltaic Stability (ISOS) condition. The limited stability exhibited by WBG PSCs under such conditions continues to be the primary obstacle hindering their practical use in tandem device applications. To confirm the benefits of the triple halide perovskite composition that we designed, we evaluated the operational stability of the corresponding devices in a custom-built high throughput aging system.[34] Devices were MPP-tracked for 1000 h at low and high temperatures under 100 mW cm$^{-2}$ light irradiation, unencapsulated in an N$_2$ atmosphere under the ISOS-L-1 and ISOS L-2 procedures (25 and 85 °C, respectively, under open-circuit), see Figure 5d, Figure S18 (Supporting Information). To further improve the stability, we replaced BCP with SnO$_X$ in the devices for MPPT analysis. The MPPT results presented below correspond to the statistical average of several cells measured simultaneously in the

**Table 1.** Photovoltaic parameters in both scan directions of the champion solar cells based on CsFA-I, CsFA-IBr, and CsFA-IBrCl compositions.

| Device | Scan direction | $V_{OC}$ [V] | $J_{SC}$ [mA cm$^{-2}$] | FF [%] | PCE [%] | Hysteresis index [%] |
|---|---|---|---|---|---|---|
| CsFA-I | Reverse | 1.09 | 24.5 | 71.9 | 19.2 | 0.13 |
| | Forward | 1.04 | 24.3 | 65.8 | 16.7 | |
| CsFA-IBr | Reverse | 1.18 | 23.1 | 75.3 | 20.6 | 0.06 |
| | Forward | 1.09 | 24.5 | 71.9 | 19.2 | |
| CsFA-IBrCl | Reverse | 1.23 | 23.1 | 79.9 | 22.6 | 0.03 |
| | Forward | 1.22 | 23.0 | 77.7 | 21.9 | |

**ADVANCED
SCIENCE NEWS**

www.advancedsciencenews.com

**ADVANCED
FUNCTIONAL
MATERIALS**

www.afm-journal.de

high throughput aging machine,[34] see Tables S5–S9 (Supporting Information), proving the reproducibility and representativity of this data. First, at 25 °C the triple halide perovskite devices retained 95% of their initial efficiency after 1000 h, see Figure 5d, showing impressive stability and a clear improvement in comparison to single (86%) and double halide devices (72%). Here, the much lower stability of the double halide perovskite highlights that, although bromide insertion can lead to high-efficiency devices, it can have dramatic consequences for the endurance of the devices, likely due to phase segregation. The introduction of the triple halide composition with chloride likely avoids this detrimental phenomenon and yields very high long-term operational stability. The average photovoltaic parameters of the devices used for the MPPT study and the number of devices used are available in Table S5 (Supporting Information).

Furthermore, we aimed to study the robustness of our compositions under temperatures as high as 85 °C (see Figure 5d), which can be reached under real operating conditions. The different devices followed a similar trend as at 25 °C, and the triple halide composition showed much higher stability, retaining an average of 74% of their initial efficiency after 1000 h, which means a huge improvement compared to single (48%) and double halide devices (51%). The swift decrease in efficiency noted in double halide perovskite in comparison to single halide counterpart is attributed to phase segregation. Nonetheless, this pattern is not sustained at temperatures <85 °C. This is because the single halide perovskite does not undergo phase segregation when exposed to light, rendering it less susceptible to degradation. Subsequently, when both CsFA-I and CsFA-IBr are exposed to elevated temperatures, phase segregation emerges as the primary factor in the degradation process, diminishing the prominence or rendering the effect of halide segregation in double halide less conspicuous. The corresponding device photovoltaic parameters and number of devices used for testing at elevated temperatures are available in Table S6 (Supporting Information), and their evolution and standard deviation in Figure S18 (Supporting Information). In the CsFA-IBrCl PSCs, we indeed detect an elevated and consistently stable Voc (open-circuit voltage). This enhancement may be linked to the effective mitigation of both non-radiative recombination processes and halide segregation within the CsFA-IBrCl perovskite films.[35,36] The triple halide devices also showed a more stable FF, compared to the more pronounced and continued loss for single and double halide perovskites. The efficiency retention was overall decent, thanks to the design of these compositions avoiding any MA content, ensuring improved long-term stability at high temperatures. In addition, to the best of our knowledge, our triple halide MA-free WBG p-i-n perovskite solar cell presented the best operational stability at high temperatures reported so far among its types. The introduction of chloride and careful design of the perovskite composition and cell structure would probably avoid not only phase segregation and material degradation but also other side reactions and detrimental processes from the rest of the device interfaces and components.

We also measured the MPPT of the triple halide perovskite device at an intermediate temperature of 65 °C, see Figure S19a and Table S7 (Supporting Information), finding as well a very high-efficiency retention of 89% after 1000 h. Finally, we tested the stability of devices with three different F-based interlayers (NaF,

KF, and LiF) deposited by thermal evaporation on top of the perovskite film. Interlayer engineering attracts a lot of interest as a key strategy to reduce non-radiative recombination losses and improve the charge transport. The photovoltaic parameters of the resulting devices are available in Table S8 (Supporting Information). We measured the stability of the devices at varying temperatures, see Figure S19b, Table S9 (Supporting Information). NaF-containing devices showed decent stability, retaining ≈80% of their initial efficiency after the stress was applied. Thus, the combination of the triple halide composition presented here with appropriate interfacial modification has enormous potential for the fabrication of long-term durable WBG perovskite solar cells. Additionally, CsFA-IBrCl perovskite material exhibited exceptional stability during testing in open-air conditions with relative humidity (RH) of 80% after 350 h according to ISOS protocols (Figure S20, Supporting Information). Our research indicates that this material is highly promising for use in tandem silicon-perovskite solar cells due to its optimal stability and performance properties. To further verify the stability of our perovskite compositions and potential degradation mechanisms, we conducted Fourier-transform infrared spectroscopy (FTIR) experiments on the CsFA-I, CsFA-IBr, and CsFA-IBrCl perovskite films, with and without thermal post-treatment at 85 and 150 °C during 10 min, though we did not observe any significant change in the spectra (Figure S21, Supporting Information). FTIR has proven highly useful in characterizing the decomposition of unstable organic components, mainly methylammonium.[37,38] However, our samples contain structurally and chemically stable compositions based on CsFA A-site cations. The main degradation source affecting our samples is the halide segregation, which implies no organic material degradation. Further decomposition processes such as hydration of the organic material[39] were also considered and could be linked to the increase in intensity of the peak at 3400 cm$^{-1}$, though the change is not significant.

In order to get additional insight into the temperature-induced degradation, impedance spectroscopy under 0.1 sun illumination was measured before and after an extreme treatment of 1 h exposure to 120 °C. The results were adjusted using an equivalent circuit reported elsewhere,[40] where the recombination processes are modeled by a resistor ($R_{rec}$), considering transport resistance negligible,[40] the device geometric capacitance is modeled by a parallel capacitor ($C_g$), and a parallel circuit with a resistor and capacitance ($R_{dr}$ and $C_{dr}$ respectively) depend on the ionic behavior. The $R_{rec}$ of CsFA-IBrCl samples is significantly higher, see **Figure 6a**, indicating lower non-radiative recombination, in agreement with the higher open circuit potential observed. Interestingly, the thermal stress has minimal effects in the recombination of samples with one and three halides. However, the recombination rate increases for the double halide sample after the treatment at 120 °C, probably by an induced halide segregation. The reduction of $R_{dr}$ after the treatment is clear for the single and double halide samples, see Figure 6b, indicating an increase of the ion vacancy density,[41] while no significant change is observed for the triple halide, which remains as the sample with the lowest ionic density before and after the treatment. Thus, temperature-induced degradation has a double effect on non-triple-halide samples: it increases recombination in the double-halide sample and increases the ion vacancy density in the single-halide sample. Chloride ions potentially occupy halide
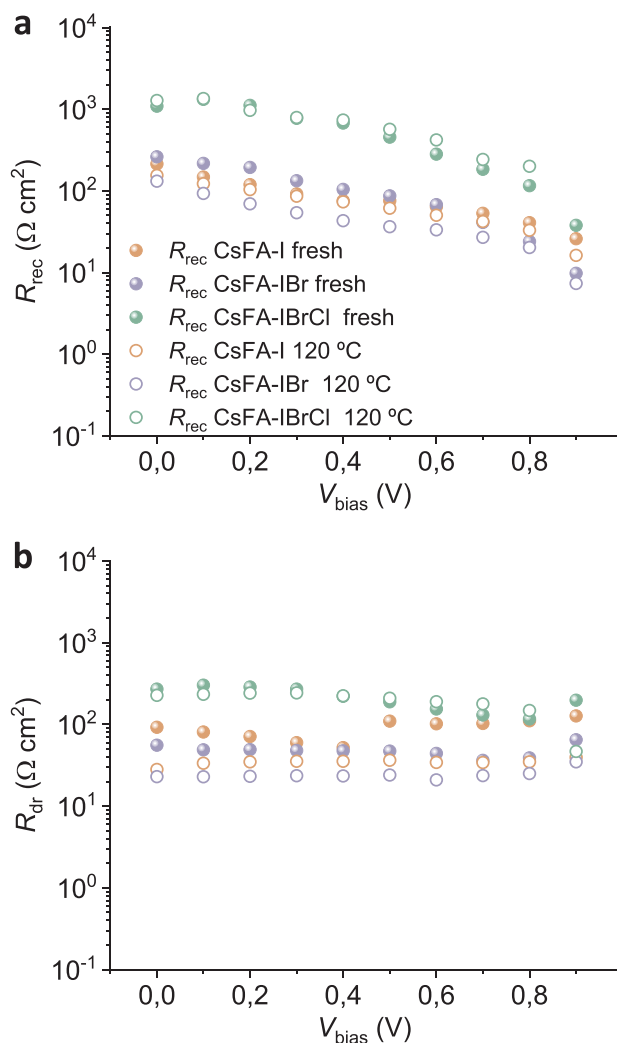
**ADVANCED**
**SCIENCE NEWS**

www.advancedsciencenews.com

**ADVANCED**
**FUNCTIONAL**
**MATERIALS**

www.afm-journal.de

**Figure 6.** a) Recombination resistance and b) ionic-related resistance extracted from impedance spectroscopy for the studied perovskite compositions before and after 120 °C treatment.

vacancies, leading to an increase in $R_{dr}$, and helping in avoiding halide segregation. Therefore, triple halide compositions successfully avoid these degradation phenomena, highlighting once again the robustness of this perovskite composition. We additionally confirmed the ability of chloride to passivate undercoordinated centers by analyzing the dark *J–V* curves of the electron-only devices. We found that the trap densities of the CsFA-IBrCl perovskite device exhibited a decrease when compared to CsFA-I (Figure S22, Supporting Information), suggesting that there is a more efficient injection of electrons to the adjacent charge transport layers in the triple halide perovskite. Further details and discussion can be found in the supporting information.

## 3. Conclusion

We introduced chloride to Br-I halide perovskite for triple halide compositions in the fabrication of MA-free WBG (1.64 eV) p-i-n perovskite solar cells with high efficiency and ultra-high stability under low and high temperatures. The careful design of perovskite and device composition by managing chloride content can avoid critical challenges such as phase segregation, low-quality thin film processing, and reduction of non-radiative recombination. The champion devices achieved efficiencies of up to 22.6% and high retention after 1000 h at MPPT at 25°C (95%), 65°C (89%), and 85°C (74%). The present study outlines a robust methodology for the solution-based manufacture of a highly interesting perovskite material for tandem applications, which improved performance and the best long-term stability up to date for this type of perovskite and device composition.

## Supporting Information

Supporting Information is available from the Wiley Online Library or from the author.

## Acknowledgements

## Conflict of Interest

The authors declare no conflict of interest.

## Data Availability Statement

The data that support the findings of this study are available in the supplementary material of this article.

[1] T. Jesper Jacobsson, J.-P. Correa-Baena, M. Pazoki, M. Saliba, K. Schenk, M. Grätzel, A. Hagfeldt, *Energy Environ. Sci.* **2016**, *9*, 1706.

[2] E. T. Hoke, D. J. Slotcavage, E. R. Dohner, A. R. Bowring, H. I. Karunadasa, M. D. McGehee, *Chem. Sci.* **2015**, *6*, 613.

[3] S. J. Yoon, M. Kuno, P. V. Kamat, *ACS Energy Lett.* **2017**, *2*, 1507.

[4] J. Cho, P. V. Kamat, *Adv. Opt. Mater.* **2020**, *9*, 2001440.

[5] J. Bisquert, E. J. Juarez-Perez, *J. Phys. Chem. Lett.* **2019**, *10*, 5889.

[6] B. W. Park, S. I. Seok, *Adv. Mater.* **2019**, *31*, 1805337.

[7] G. E. Eperon, S. D. Stranks, C. Menelaou, M. B. Johnston, L. M. Herz, H. J. Snaith, *Energy Environ. Sci.* **2014**, *7*, 982.

[8] X.-X. Gao, W. Luo, Y. Zhang, R. Hu, B. Zhang, A. Züttel, Y. Feng, M. K. Nazeeruddin, *Adv. Mater.* **2020**, *32*, 1905502.

[9] E. J. Zheng, Z. Y. Niu, G. A. Tosado, H. Dong, Y. Albrikan, Q. M. Yu, *J. Phys. Chem. C* **2020**, *124*, 18805.

[10] J. Cho, J. T. DuBose, P. S. Mathew, P. V. Kamat, *Chem. Commun.* **2021**, *57*, 235.

[11] J. S. Cho, P. V. Kamat, *Chem. Mater.* **2020**, *32*, 6206.

[12] R. Cheng, C. C. Chung, H. Zhang, F. Liu, W. T. Wang, Z. Zhou, S. Wang, A. B. Djurišić, S. P. Feng, *Adv. Energy Mater.* **2019**, *9*, 1901980.

[13] H. C. Liao, P. J. Guo, C. P. Hsu, M. Lin, B. H. Wang, L. Zeng, W. Huang, C. M. M. Soe, W. F. Su, M. J. Bedzyk, M. R. Wasielewski, R. P. H. Chang, M. G. Kanatzidis, T. J. Marks, *Adv. Energy Mater.* **2017**, *7*, 1601660.

[14] S. Colella, E. Mosconi, P. Fedeli, A. Listorti, F. Gazza, F. Orlandi, P. Ferro, T. Besagni, A. Rizzo, G. Calestani, G. Gigli, F. De Angelis, R. Mosca, *Chem. Mater.* **2013**, *25*, 4613.

[15] M. M. Tavakoli, P. Yadav, D. Prochowicz, M. Sponseller, A. Osherov, V. Bulovic, J. Kong, *Adv. Energy Mater.* **2019**, *9*, 1803587.

[16] S. T. Williams, F. Zuo, C. C. Chueh, C. Y. Liao, P. W. Liang, A. K. Jen, *ACS Nano* **2014**, *8*, 10640.

[17] K. Odysseas Kosmatos, L. Theofylaktos, E. Giannakaki, D. Deligiannis, M. Konstantakou, T. Stergiopoulos, *Energy Environ. Mater.* **2019**, *2*, 79.

[18] J. Park, J. Kim, H. S. Yun, M. J. Paik, E. Noh, H. J. Mun, M. G. Kim, T. J. Shin, S. I. Seok, *Nature* **2023**, *616*, 724.

[19] S. Mariotti, E. Kohnen, F. Scheler, K. Sveinbjornsson, L. Zimmermann, M. Piot, F. Yang, B. Li, J. Warby, A. Musiienko, D. Menzel, F. Lang, S. Kessler, I. Levine, D. Mantione, A. Al-Ashouri, M. S. Hartel, K. Xu, A. Cruz, J. Kurpiers, P. Wagner, H. Kobler, J. Li, A. Magomedov, D. Mecerreyes, E. Unger, A. Abate, M. Stolterfoht, B. Stannowski, R. Schlatmann, et al., *Science* **2023**, *381*, 63.

[20] X. Y. Chin, D. Turkay, J. A. Steele, S. Tabean, S. Eswara, M. Mensi, P. Fiala, C. M. Wolff, A. Paracchino, K. Artuk, D. Jacobs, Q. Guesnay, F. Sahli, G. Andreatta, M. Boccard, Q. Jeangros, C. Ballif, *Science* **2023**, *381*, 59.

[21] NREL, Best Research-Cell Efficiencies chart, https://www.nrel.gov/pv/cell-efficiency.html (accessed: February 2024).

[22] C. Y. Yi, J. S. Luo, S. Meloni, A. Boziki, N. Ashari-Astani, C. Grätzel, S. M. Zakeeruddin, U. Röthlisberger, M. Grätzel, *Energy Environ. Sci.* **2016**, *9*, 656.

[23] S. H. Turren-Cruz, A. Hagfeldt, M. Saliba, *Science* **2018**, *362*, 449.

[24] R. Montecucco, E. Quadrivi, R. Po, G. Grancini, *Adv. Energy Mater.* **2021**, *11*, 2100672.

[25] Z. Liu, C. Zhu, H. Luo, W. Kong, X. Luo, J. Wu, C. Ding, Y. Chen, Y. Wang, J. Wen, Y. Gao, H. Tan, *Adv. Energy Mater.* **2023**, *13*, 2203230.

[26] A. Z. Afshord, B. E. Uzuner, W. Soltanpoor, S. H. Sedani, T. Aernouts, G. Gunbas, Y. Kuang, S. Yerci, *Adv. Funct. Mater.* **2023**, *33*, 2301695.

[27] R. A. Kerner, Z. J. Xu, B. W. Larson, B. P. Rand, *Joule* **2021**, *5*, 2273.

[28] H. K. Zhang, W. Yu, J. X. Guo, C. Xu, Z. W. Ren, K. Liu, G. Yang, M. C. Qin, J. M. Huang, Z. L. Chen, Q. Liang, D. Shen, Z. H. Wu, Y. K. Zhang, H. T. Chandran, J. H. Hao, Y. Zhu, C. S. Lee, X. H. Lu, Z. J. Zheng, J. S. Huang, G. Li, *Adv. Energy Mater.* **2022**, *12*, 2201663.

[29] B. Roose, K. Dey, Y. H. Chiang, R. H. Friend, S. D. Stranks, *J. Phys. Chem. Lett.* **2020**, *11*, 6505.

[30] B. W. Park, N. Kedem, M. Kulbak, D. Y. Lee, W. S. Yang, N. J. Jeon, J. Seo, G. Kim, K. J. Kim, T. J. Shin, G. Hodes, D. Cahen, S. I. Seok, *Nat. Commun.* **2018**, *9*, 3301.

[31] W. Mao, C. R. Hall, S. Bernardi, Y. B. Cheng, A. Widmer-Cooper, T. A. Smith, U. Bach, *Nat. Mater.* **2021**, *20*, 55.

[32] J. Xu, C. C. Boyd, Z. J. Yu, A. F. Palmstrom, D. J. Witter, B. W. Larson, R. M. France, J. Werner, S. P. Harvey, E. J. Wolf, W. Weigand, S. Manzoor, M. van Hest, J. J. Berry, J. M. Luther, Z. C. Holman, M. D. McGehee, *Science* **2020**, *367*, 1097.

[33] A. Al-Ashouri, A. Magomedov, M. Ross, M. Jost, M. Talaikis, G. Chistiakova, T. Bertram, J. A. Márquez, E. Köhnen, E. Kasparavicius, S. Levcenco, L. Gil-Escrig, C. J. Hages, R. Schlatmann, B. Rech, T. Malinauskas, T. Unold, C. A. Kaufmann, L. Korte, G. Niaura, V. Getautis, S. Albrecht, *Energy Environ. Sci.* **2019**, *12*, 3356.

[34] H. Köbler, S. Neubert, M. Jankovec, B. Glažar, M. Haase, C. Hilbert, M. Topič, B. Rech, A. Abate, *Energy Technol.* **2022**, *10*, 2200234.

[35] S. Mahesh, J. M. Ball, R. D. J. Oliver, D. P. Mcmeekin, P. K. Nayak, M. B. Johnston, H. J. Snaith, *Energy Environ. Sci.* **2020**, *13*, 258.

[36] A. J. Knight, J. B. Patel, H. J. Snaith, M. B. Johnston, L. M. Herz, *Adv. Energy Mater.* **2020**, *10*, 1903488.

[37] G. Abdelmageed, C. Mackeen, K. Hellier, L. Jewell, L. Seymour, M. Tingwald, F. Bridges, J. Z. Zhang, S. Carter, *Sol. Energy Mater. Sol. Cells* **2018**, *174*, 566.

[38] D. Yerezhep, Z. Omarova, A. Aldiyarov, A. Shinbayeva, N. Tokmoldin, *Molecules* **2023**, *28*, 1288.

[39] Z. Zhu, V. G. Hadjiev, Y. Rong, R. Guo, B. Cao, Z. Tang, F. Qin, Y. Li, Y. Wang, F. Hao, S. Venkatesan, W. Li, S. Baldelli, A. M. Guloy, H. Fang, Y. Hu, Y. Yao, Z. Wang, J. Bao, *Chem. Mater.* **2016**, *28*, 7385.

[40] S. M. Yoo, S. J. Yoon, J. A. Anta, H. J. Lee, P. P. Boix, I. Mora-Seró, *Joule* **2019**, *3*, 2535.

[41] A. J. Riquelme, K. Valadez-Villalobos, P. P. Boix, G. Oskam, I. Mora-Sero, J. A. Anta, *Phys. Chem. Chem. Phys.* **2022**, *24*, 15657.